Environmental Science & Technology

Article

pubs.acs.org/est

Bacterially Produced Calcium Phosphate Nanobiominerals: Sorption Capacity, Site Preferences, and Stability of Captured Radionuclides

S. Handley-Sidhu,*[,†,‡] J. A. Hriljac,[§] M. O. Cuthbert,[†,∥] J. C. Renshaw,[⊥] R. A. D. Pattrick,[#] J. M. Charnock,[#] B. Stolpe,[†] J. R. Lead,[†,▲] S. Baker,[†] and L. E. Macaskie[‡]

[†]School of Geography Earth and Environmental Sciences, [‡]School of Biosciences, [§]School of Chemistry, The University of Birmingham, Edgbaston, Birmingham B15 2TT, U.K.

[∥]Connected Waters Initiative Research Centre, The University of New South Wales, King Street, Manly Vale, New South Wales 2093, Australia

[⊥]Department of Civil and Environmental Engineering, University of Strathclyde, Glasgow G1 1XQ, U.K.

[#]School of Earth, Atmospheric and Environmental Sciences, The University of Manchester, Oxford Road, Manchester M13 9PL, U.K.

[▲]Center for Environmental Nanoscience and Risk, Arnold School of Public Health, University of South Carolina, Columbia, South Carolina 29208, United States

Supporting Information

ABSTRACT: A *Serratia* sp. bacterium manufactures amorphous calcium phosphate nanominerals (BHAP); this material has shown increased sorption capacity for divalent radionuclide capture. When heat-treated (≥450 °C) the cell biomass is removed and the biominerals are transformed to hydroxyapatite (HAP). Using a multimethod approach, we have elucidated both the site preferences and stability of analogue radionuclide incorporation for Sr, Co, Eu, and U. Strontium incorporates within the bulk amorphous inorganic phase of BHAP; however, once temperature modified to crystalline HAP, bonding was consistent with Sr substitution at the Ca(1) and/or Ca(2) sites. Cobalt incorporation occurs within the bulk inorganic amorphous phase of BHAP and within the amorphous grain boundaries of HAP. Europium (an analogue for trivalent actinides) substituted at the Ca(2) and/or the Ca(3) position of tricalcium phosphate, a known component of HAP grain boundaries. Uranium was surface complexed with no secondary minerals detected. With multiple sites for targeted radionuclide incorporation, high loadings, and good stability against remobilization, BHAP is shown to be a potential material for the remediation of aqueous radionuclide in groundwater.

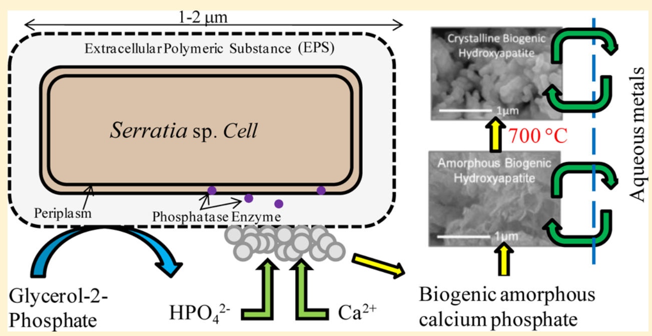

Apatites, general formula $[Ca_5(PO_4)_3(OH,F,Cl)]$, are suitable materials for radioactive waste cleanup, storage, and disposal because they can incorporate radionuclides within their structures, are very stable in the geosphere, and are resistant to radiation damage.[1−3]

Serratia sp. cells (originally isolated as a *Citrobacter* sp. from a heavy metal contaminated land site)[4] contain high levels of an atypical phosphatase; this enzyme cleaves inorganic PO_4^{3-} from an organic phosphate substrate, and, in the presence of Ca^{2+}, the cell surface microenvironment and solution phase become supersaturated, producing an amorphous calcium phosphate biomineral (BHAP; see Figure 1).[2,5] BHAP is a promising remediation material with higher sorption capacities (up to 15 times higher) for Sr^{2+} and Co^{2+} than that of commercially produced hydroxyapatite (HAP); the specific morphology (i.e., smaller crystallite size (<40 nm) and higher specific surface area (>70 m^2 g^{-1})) was shown to underlie these advantages.[6] The addition of citrate during HAP inhibits crystal growth by binding onto mineral surfaces.[7,8] In laboratory studies, BHAP produced with citrate was 7 times more efficient than commercial HAP in removing Sr^{2+} from an artificial groundwater.[2]

HAP materials are polycrystalline structures with grain boundaries containing amorphous calcium phosphate species.[9] In crystalline HAP $[Ca_{10}(PO_4)_6(OH_2)]$, ten calcium cations are aligned in two nonequivalent sites denoted as Ca(1) and Ca(2) (9- and 7-fold coordinated, respectively); these sites are the target for divalent cation substitution (e.g., Sr^{2+}, Zn^{2+}, Cr^{2+}),[10] whereas recent evidence suggests that trivalent actinides (such as, Cm^{3+}) are held within the amorphous grain boundaries.[11] Tricalcium phosphate [TCP; $Ca_3(PO_4)_2$], a known component of HAP grain boundaries,[12] has five nonequivalent calcium cations: Ca(1) is 7-fold coordinated, Ca(2) and Ca(3) are 8-

Received: February 12, 2014
Revised: May 7, 2014
Accepted: May 13, 2014
Published: May 13, 2014

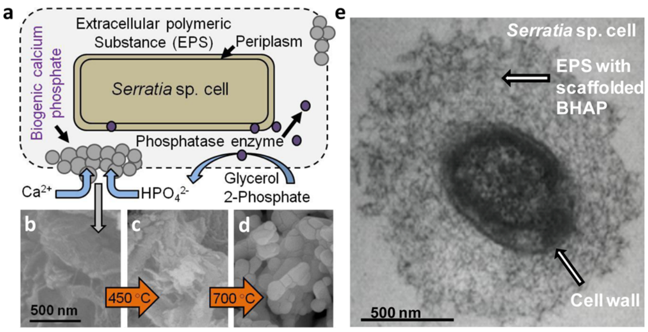

Figure 1. Showing **a** the conceptual mechnism of amorphous calcium phsophate formation. Backscattered SEM images of **b** initial-BHAP, **c** 450-BHAP, and **d** 700-BHAP (80,000× magnification; 500 nm size bar). TEM image of **e** Serratia sp. cell with scaffolded BHAP on the EPS (50,000× magnification; 500 nm size bar).

fold coordinated, Ca(4) is 3-fold coordinated, and Ca(5) is 6-fold coordinated.[13]

Although BHAP has shown promise for radionuclide capture and storage, these materials can contain between 5 and 50% cell biomass.[6] This high organic content is not suitable for remediation technologies as its biodegradation could lead to the remobilization of organic-adsorbed radionuclides via the production of organic acids and chelating agents.[14] Removal of associated organics using heat treatment prior to remediation is an option. However, thermal annealing may modify the structure of BHAP,[15] and this may, in turn, influence sorption capacity and the stability of incorporated metals.

Analogue radionuclides were used in this study: ^{90}Sr, ^{60}Co, and $^{238}U/^{235}U$ which are contributors to radioactivity in nuclear wastes and environmental contamination associated with nuclear energy and weapons production. Europium is a minor contributor to nuclear waste and an analogue for the more problematic and highly active trivalent actinides, such as *Cm*.

We have previously demonstrated that BHAP has increased capacity for divalent radionuclide sorption when compared to synthetic counterparts.[6] In this study we have included analogue actinides and used a multimethod characterization approach to determine the site of radionuclide (Sr^{2+}, Co^{2+}, Eu^{3+}, UO_2^{2+}) incorporation and stability against remobilization; thus, establishing BHAP as a possible material for environmental remediation technologies.

■ METHODS

Hydroxyapatite Material. BHAP was manufactured using *Serratia* sp. (NCIMB 40259, Isis Innovation, Oxford, UK). Four flasks containing 1 L of 0.1 M AMPSO buffer (pH 8.6) and *Serratia sp.* (OD_{600} = 1.0 mg dry biomass/mL) were inoculated daily with 2 mM $CaCl_2$, 2 mM sodium citrate, and 5 mM glycerol 2-phosphate. Flasks were incubated (30 °C) and shaken (100 rpm). After 8 days the BHAP was harvested by centrifugation, air-dried, then manually ground, and sieved to <105 μm. HAP-1 (Sigma-Aldrich; Part number: 677418) was used for comparison.[6] Subsamples of BHAP were heated for 2 h at a single temperature of 200, 250, 300, 350, 400, 450 500, 550, 600, 650, and 700 °C, and the loss of organic mass was recorded by weight. Subsamples are abbreviated as initial-BHAP (no heat-treatment) and from 200-BHAP to 700-BHAP to denote treatment temperature.

Material Characterization. BHAP and reference samples were analyzed by XRD (Bruker D8 advanced X-ray diffractometer; Cu Kα radiation). The crystallite size was calculated from the characteristic peak at 2θ = 26° (corresponding to 002 plane) using the Scherrer equation[16] (eq S1).

The specific surface area (SSA) was determined using a BET surface area analyzer (Beckman Coulter, SA 3100). A sample (0.05−0.1 g ± 0.0005 g) was weighed and outgassed at 190 °C for 12 h prior to analysis.

High resolution micrographs were obtained using scanning electron microscopy (SEM; Philips XL30) and transmission electron microscopy (TEM; Jeol 1200-EX). For SEM, BHAP mounted onto stubs were platinum-coated, and the secondary electron and backscattering micrographs were obtained at 15 keV. For TEM, BHAP water suspensions (10 mg L^{-1}) were deposited onto a 300 mesh Formvar coated Cu-grids using ultracentrifugation (Beckman L-75, 30000 rpm; 60 min), rinsed in deionized water (≤18.2 MΩ/cm), and air-dried. Whole cells (day 3 of BHAP mineralization) were harvested by centrifugation (6000 rpm; 10 min), fixed (2.5% glutaraldehyde in 0.1 M sodium cacodylate/HCl buffer pH 7.2) at 4 °C (1 h), dehydrated at room temperature, osmium-stained, sectioned, and examined. All TEM micrographs were acquired at 80 keV. The sizes (equivalent circular diameter) and aspect ratios (breadth/length ratio) were determined (16 to 176 particles) using image analysis software (Digital Micrograph, Gatan Inc.).

Sorption of Aqueous Radionuclide. Solutions were prepared using $SrCl_2$, $CoCl_2$, $EuCl_3$, and $UO_2(NO_3)_2$ salts and deionized water to give final concentrations of 10.3 mM; the solution pH was adjusted using NaOH so that the final values were between pH 5−6. Within this pH range, the sorption of metals and HAP stability is constant (<1% relative standard deviation, data not shown). All sorption experiments were carried out in triplicate. Accurately weighed masses (∼0.02 g) of BHAP and reference samples were placed in 3 mL polypropylene vials, and an aliquot (2000 μL) of the appropriate solution was added and shaken to suspend the solid. The vials were immediately positioned vertically on an orbital shaker (100 rpm) at room temperature (24 h is sufficient for equilibrium, kinetic data not shown), samples were then harvested by centrifugation (16,000 g; 30 min; Sigma 1-14), and the supernatant was analyzed by ion chromatography (Dionex, ICS-1100) to determine the residual solution phase concentrations of Sr, atomic absorption spectroscopy (AAS; PerkinElmer, AAnalyst 300) for solution phase Co, and inductively coupled plasma mass spectroscopy (ICP-MS; Agilent 7500ce) for solution phase Eu and U. All results are reported as mmol 100 g^{-1} (Supporting Information eq S2). The geochemical model visual MINTEQ version 3.1[17] was used to determine metal speciation with measured water chemistry (pH, ions conc.).

Radionuclide Analogue Incorporation. X-ray absorption spectroscopy (XAS) data were collected at the Co K-edge, the Sr K-edge, and the Eu L_{II}-edge (chosen rather than the Eu L_{III}-edge to avoid interference from trace Fe), on beamline I18 at the Diamond Light Source, UK. In this study, a cryo-cooled Si(111) double crystal monochromator was used and calibrated for energy using a Co foil for the Co and Eu edges and $Sr(CO_3)$ for the Sr edge recorded in transmission mode. Data for the samples were collected in fluorescence mode using an Ortec 9-element Ge detector. Two scans were recorded and averaged for the transmission samples, with either four or eight

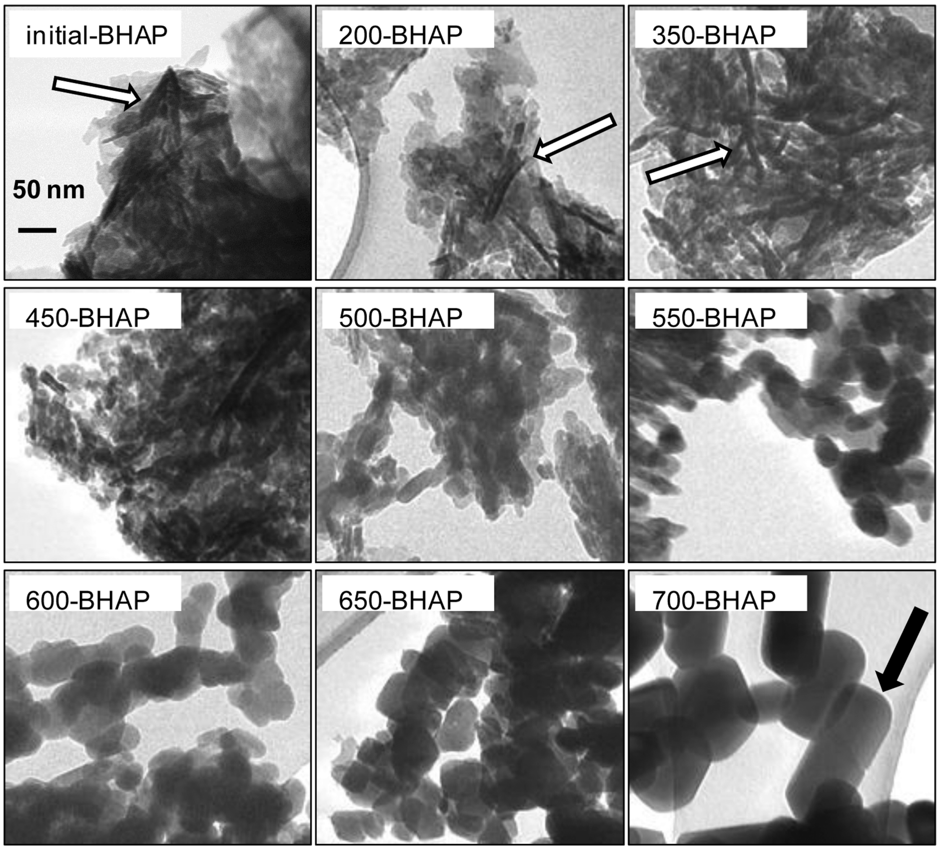

Figure 2. Selected TEM images of initial-BHAP and selected heat treated BHAP materials (300,000× magnification; 50 nm size bar shown). White arrows highlight fiber-like structures; black arrows highlight the formation of larger "rounded off" elongated particles with an increased domain size and higher aspect ratios.

scans for fluorescence data. For each set of scans the repeat spectra were compared with the initial scan. There was no indication of any changes in the edge position or shape, nor any differences in the EXAFS oscillations for the samples analyzed.

XANES data were extracted by fitting a first order polynomial to the pre-edge and two smoothly joining third order polynomials to the postedge region of the XAS data. These were subtracted from the spectrum and the edge-jump normalized to 1. XANES spectra were compared in the ranges 7690−7850 eV (Co K-edge), 16090−16200 (Sr K-edge), and 7600−7750 eV (Eu LII-edge). Background subtracted and normalized EXAFS spectra were analyzed using exact curved wave theory[18] in DL-Excurv.[19] Phaseshifts were derived in the program from *ab initio* calculations using Hedin-Lundqvist potentials and von Barth ground states.[20] The data were fitted for each sample by defining a theoretical model and comparing the calculated EXAFS spectrum with the experimental data. Shells of backscatterers were added around the central absorber atom and by refining (i) an energy correction (Ef, Fermi energy); (ii) the absorber-scatterer distance, and (iii) the Debye−Waller factor for each shell; a least-squares residual (R-factor[21]) was minimized. For the Co and Sr analyses the number of scatterers in each shell was initially refined and then fixed as the closest integer values. For Eu, due to the shorter data range limiting the number of independent points, arbitrary values were chosen for N based on the structure of $Eu(PO_4)$ and were not refined. For each shell of scatterers included beyond the first, a reduced chi-squared test was used to ensure that the improvement in fit with the additional parameters was statistically justified.

Selected BHAP samples (initial-BHAP, 450-BHAP, 700-BHAP), HAP-1, and β-TCP were analyzed. Samples were also heat-treated (amorphous phase transforms to a more crystalline material) to 700 °C after metal sorption to give additional information on metal incorporation. These samples are denoted with an asterisk (e.g., *initial-BHAP). Uranium samples were not analyzed due to surface complexation being the reported mechanism of association.[22]

Remobilization of Incorporated Radionuclide Analogues. Selected BHAP samples (initial-BHAP, 450-BHAP, and BHAP-700) were tested for their ability to retain incorporated metals in groundwater. Solid samples from the previous sorption study were air-dried, and accurately weighed powders (~0.02 g) were placed in clean 3 mL polypropylene vials. An aliquot (2000 μL) of artificial groundwater (pH 7.6)[23] was added, and the vials were shaken (100 rpm) at room temperature (24 h); solution samples were then harvested and analyzed for released metals as previously described.

RESULTS AND DISCUSSION

Biomineral samples are abbreviated as initial-BHAP (no heat-treatment) and from 200-BHAP to 700-BHAP to denote the treatment temperature. Scanning electron microscopy analysis (SEM; Figure 1 and Supporting Information Figure S1) showed that the initial-BHAP and BHAP heat-treated up to 450 °C consisted of plate-like layered structures, whereas 700-BHAP consisted of agglomerated particles (50−300 nm in

dx.doi.org/10.1021/es500734n | *Environ. Sci. Technol.* 2014, 48, 6891−6898

size). Transmission electron microscopy (TEM) images and data (Figure 2, Figure 3a) of initial-BHAP to 450-BHAP reveal

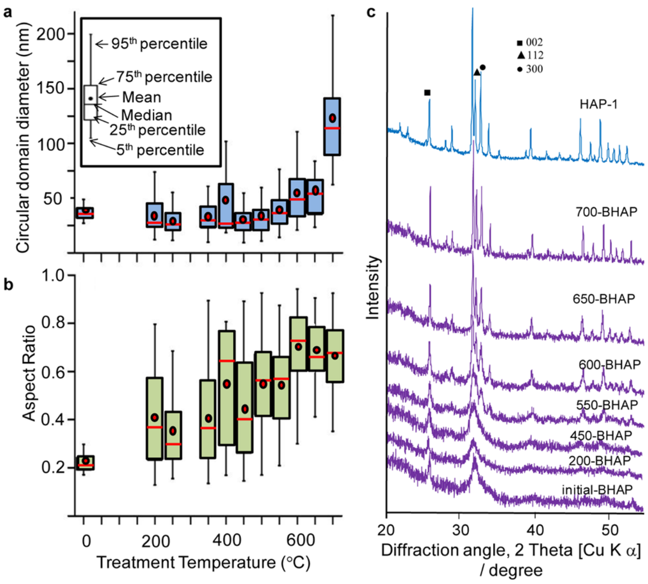

Figure 3. Data determined from the TEM micrographs showing **a** variations in domain size distribution (equivalent spherical diameter) and **b** aspect ratio (breadth/length) of discrete hydroxyapatite nanoparticles (n = between 18 and 176 particles measured for each treatment temperature). XRD patterns **c** showing reference sample HAP-1 and changes in BHAP crystallinity with increasing temperatures treatments.

that the plate structures are formed of nanofibrous structures, suggesting that BHAP nanoparticles are templated on the organic framework of the extracellular polymeric substance (as shown in Figure 1e).[24] Temperature treatments promoted the transformation of the fiber-like structures (Figure 2, BHAP samples heat treated up to 350 °C, white arrows) and resulted in the formation of larger "rounded off" elongated particles with an increased domain size (>100 nm for 700- BHAP) and higher aspect ratios (black arrows, Figure 3b). The X-ray powder diffraction (XRD) patterns for BHAP (Figure 3c) were matched against calcium hydrogen phosphate hydroxide (JCPDS database; pattern number 00-046-0905). The initial-BHAP showed ill defined and broad peaks indicative of amorphous and/or nanoparticulate material,[6] becoming progressively better defined (increased structural ordering) with heat treatment ≥500 °C. By 700 °C the XRD pattern closely matched that of HAP-1 (Figure 3c) with additional peaks (0210, 128, and 1112) corresponding to TCP (JCPDS database, pattern number 00-009-0169; Supporting Information Figure S2). The average crystallite size (calculated by the Scherrer equation, Supporting Information eq S1) ranged from 32 to 40 nm for ≤500-BHAP samples (Table 1). Above 550 °C, the average crystallite size (Table 1) increased from 48 to 271 nm at 700 °C. The SSA also varied with heat treatment (Table 1), increasing from 65 ± 2 $m^2\ g^{-1}$ (200-BHAP) to 115 ± 4 $m^2\ g^{-1}$ (400-BHAP). This correlates with the removal of organics (r^2 = 0.97) leading to an increase in void spaces and a subsequent increase in SSA[15]. The SSA then decreased with increasing heat treatments to 12 ± 4 $m^2\ g^{-1}$ (700-BHAP), consistent with the enlargement of XRD crystallite and TEM domain sizes[25] (Figure 2, Figure 3). The organic content which is attributed to *Serratia* sp. biomass decreased with heat treatment from 36% (initial-BHAP) to 3% at 450 °C (Table 1).

Table 1. Showing % Weight Loss on Ignition, BET Specific Surface Area, Average XRD Crystallite Size, and Sorption Data[a]

sample	organic content (wt %)	surface area ($m^2\ g^{-1}$)	XRD crystallite size (nm)	adsorption (mmol 100 g^{-1}) Co^{2+}	Sr^{2+}	Eu^{3+}	UO_2^{2+}
initial-BHAP	36		40	97	41	154	131
200-BHAP	27	65	34	89	41	154	131
250-BHAP	23	76	37	87	38	154	131
300-BHAP	16	93	33	78	38	154	131
350-BHAP	9	102	37	75	38	154	131
400-BHAP	7	115	36	77	38	154	131
450-BHAP	3	86	36	67	34	154	131
500-BHAP	3	61	32	53	27	154	131
550-BHAP	1	38	48	38	22	154	131
600-BHAP	2	27	64	42	26	154	131
650-BHAP	0	17	125	25	19	153	124
700-BHAP	0	12	271	16	15	151	116
HAP-1	0	21	85	18	18	13	130

[a]Error ± <5% relative standard deviation and N = 3.

The characterization of HAP-1 by SEM revealed rounded particles of varying sizes (≤100 μm, Figure S1); further analysis by TEM showed that these particles were made up of agglomerated particles (mean TEM domain size <50 nm). XRD pattern analysis confirmed that HAP-1 is a crystalline HAP material (no characteristic β-TCP peaks were observed). This material had a relatively low SSA (21 ± 1) and large XRD crystallite size (85 nm) (Figure S1, Table 1) when compared to BHAP. Heating to 700 °C did not significantly change the structure of HAP-1 (as indicated by XRD, data not shown).

Removal of aqueous metal ions by BHAP is shown in Table 1. A small amount of observed Sr^{2+} and UO_2^{2+} removal was attributed to precipitation from measured solution phase phosphate (i.e., < 0.2% $SrH_2PO_4^+$ and <1% $UO_2PO_4^-$).[17] The sorption of Co^{2+} decreased on materials that were heat treated, from 97 ± 1 mmol/100 g (initial-BHAP) to 16 ± 3 mmol/100 g for 700-BHAP (Pearson's coefficient −0.95). The characterization data shows that for temperature treatments of ≤400 °C, the bulk organic biomass can be removed without notably modifying the structure of BHAP; therefore, any changes in metal sorption from initial-BHAP to 400-BHAP is related to % organic content. There is a strong correlation between organic content and Co^{2+} sorption (see Table 1; initial-BHAP to 400-BHAP; Pearson's coefficient 0.97); with approximately 20% of the total Co^{2+} associated with the organic phase of initial-BHAP. The sorption of Sr^{2+} (Table 1) also decreased with heat treatment from 41 ± 1 (initial-BHAP) to 15 ± 4 mmol/100 g for 700-BHAP (Pearson's coefficient −0.91). Similarly, there is a strong correlation between organic

Table 2. Parameters Obtained from EXAFS Data Fitting of Sr K-Edge, Co K-Edge, and Eu L-Edge Spectra of Metals Associated with Biological, Synthetic Hydroxyapatite, and Reference Samples[a]

sample	cobalt S	cobalt N	cobalt r (A)	cobalt $2\sigma^2$ (A^2)	cobalt R	strontium S	strontium N	strontium r (A)	strontium $2\sigma^2$ (A^2)	strontium R	europium S	europium N	europium r (A)	europium $2\sigma^2$ (A^2)	europium R
$SrCO_3$						O	9	2.62	0.025	25.1					
						C	3	3.05	0.014						
						C	3	3.45	0.045						
						Sr	4	4.18	0.024						
						Sr	6	4.60	0.033						
β tricalcium phosphate (β-TCP) $Ca_3(PO_4)_2$	O	5	2.02	0.031	31.4	O	7	2.57	0.029	42.0	O	8	2.44	0.023	16.2
	P	1	3.00	0.004							P	8	3.18	0.055	
	P	2	3.23	0.012							Eu	6	4.12	0.036	
HAP-1	O	4	1.94	0.025	24.7	O	7	2.58	0.024	35.7	O	8	2.43	0.025	13.8
	P	2	2.99	0.008							P	8	3.20	0.086	
	P	2	3.22	0.005							Eu	6	4.19	0.057	
initial-BHAP	O	5	2.02	0.033	27.2	O	7	2.58	0.030	29.7	O	8	2.44	0.025	17.7
	P	2	3.25	0.047		P	4	3.26	0.047		P	8	3.18	0.056	
											Eu	6	4.09	0.035	
450-BHAP	O	5	2.01	0.033	29.1	O	7	2.58	0.030	30.3	O	8	2.44	0.025	16.8
	P	1	3.04	0.013		P	4	3.26	0.043		P	8	3.18	0.054	
	P	1	3.25	0.008							Eu	6	4.12	0.032	
700-BHAP	O	5	2.02	0.031	26.3	O	7	2.53	0.028	34.0	O	8	2.44	0.024	20.8
	P	2	3.26	0.039		P	4	3.23	0.031		P	8	3.18	0.056	
						O	8	3.99	0.035		Eu	6	4.10	0.035	
*initial-BHAP (heat treated at 700 °C; 2 h) after metal sorption	O	4	2.01	0.019	24.1	O	7	2.54	0.031	35.9	O	8	2.43	0.031	23.0
						P	4	3.24	0.028		P	8	3.18	0.057	
						Ca	4	4.12	0.034		Eu	6	4.21	0.031	
*HAP-1 (heat treated at 700 °C; 2 h) after metal sorption	O	4	1.92	0.004	26.8	O	7	2.55	0.028	33.8	O	8	2.42	0.027	16.2
	Co	4	2.86	0.009		P	4	3.24	0.030		P	8	3.20	0.087	
	Co	4	3.37	0.001		Ca	4	4.13	0.036		Eu	6	4.21	0.049	
	Co	6	4.99	0.006											

[a]S is the scatterer type, N is the number of scatterers ±25%, r (Å) is the absorber-scatterer distance ±0.02 Å inner shell, ±0.05 Å outer shells, $2\sigma^2$ (Å^2) is the Debye−Waller factor ±25%, and R is a least-squares residual.

content and Sr^{2+} sorption (initial-BHAP to 400-BHAP; Pearson's coefficient 0.82); with approximately 7% of total Sr^{2+} associated with the organic phase of initial-BHAP. Despite the reduction in divalent metal sorption (from initial-BHAP to 700-BHAP) with heat treatment, results show that the sorption of Co^{2+} and Sr^{2+} in BHAP are significantly higher (up to 5 and 2 times higher, respectively) than those of HAP-1 (classified by Sigma-Aldrich as a HAP nanopowder) tested (see Table 1). The sorption of Eu^{3+} did not change significantly with the heat treatment (154 ± 1 mmol/100 g), due to adsorption sites not being fully saturated. The sorption of UO_2^{2+} decreased slightly after treatment >600 °C from 131 ± <1 for initial-BHAP to 116 ± 2 mmol/100 g for 700-BHAP, due to the reduction in surface area. In comparison, the reference HAP-1 sample had similar UO_2^{2+} sorption of 130 ± <1 mmol/100 g but a significantly lower (up to 12 times) Eu^{3+} sorption of 13 ± 5 mmol/100 g.

XRD Studies. Near identical XRD patterns were produced from the reference sample (HAP-1 and 700-BHAP) and the 700-BHAP with adsorbed Co^{2+} (1.0 g/100 g), Sr^{2+} (1.3 g/100 g), Eu^{3+} (23.0 g/100 g), and UO_2^{2+} (27.6 g/100 g) (Supporting Information Figure S3, Figure 3). El Kabouss et al.[26] reported identical XRD patterns for HAP and Hap with ≤1.7 g/100 g Co^{2+}, whereas, at concentrations ≥1.7 g/100 g Co^{2+}, a characteristic (311) Co_3O_4 peak appeared. In this study, no change in the XRD pattern for HAP-Co is expected at the extent of sorption observed. Strontium adsorbed onto the 700-BHAP (1.3 g/100 g) and the control sample were also analyzed by XRD. The patterns (Figure S3) were both matched against calcium hydrogen phosphate hydroxide and calcium strontium phosphate hydroxide (JCPDS database; pattern number 00-046-0905 and 00-060-0647, respectively), showing that the mineral phases cannot be distinguished. For Eu^{3+}, it is feasible for the smaller ionic radius (1.01 and 1.12 Å for 7-fold and 9-fold coordination[27]) to substitute at the Ca(1) and Ca(2) positions of HAP.[28] However, in this study no change in the XRD pattern was observed for BHAP-700 with 23.0 g/100 g adsorbed Eu^{3+} (Figure S3). Recent work by Holliday et al.[11] using time-resolved laser fluorescence spectroscopy (TRLFS) ruled out both surface complexation and incorporation into the Ca(1) and Ca(2) sites of HAP and concluded that Eu^{3+} incorporation occurs within the grain boundaries of polycrystalline HAP. Fuller et al.[22] completed a comprehensive investigation into the mechanism of U(VI) sorption onto synthetic HAP using extended X-ray absorption fine structure (EXAFS). Uranium loadings of 0.7 g/100 g were attributed to surface complexation, whereas loadings of 4 g/100 g closely matched the formation of autunite and chernikovite. For BHAP-700 with 27.6 g/100 g loadings, the lack of uranium phosphate phases (e.g., chernikovite) detected by XRD (Figure S3) suggests that surface complexation instead of precipitation has occurred. This is in accordance with the previous work of Fuller et al.[29] which also reported that the presence of carbonate in biological apatite suppresses the formation of chernikovite on HAP. For UO_2^{2+}, no further analyses using X-ray absorption spectroscopy (XAS) were carried out because surface complexation has previously been determined as mechanism of removal.[22]

Co K-edge, X-ray absorption near edge structure (XANES) spectra of the materials reacted with Co^{2+} are shown in Supporting Information Figures S4 a-c. The XANES spectra of the Co sorbed to the reference samples (HAP-1 and β-TCP) have similar peak shape and energies, indicating similar coordination, consistent with Co(II) (edge energy of 7719 eV and a white line at 7724.5 eV). The XANES spectra derived from the biogenic samples (initial-BHAP, 450-BHAP, 700-BHAP) are comparable and similar to the spectra in the reference samples, with edge energies of 7719 EV and white lines at 7724 eV. The XANES spectra of the samples heated to 700 °C after Co sorption show differences (denoted with *). The *HAP-1 absorption edge is at a higher energy (7722 eV) with two additional features on the edge, and a white line (7729 eV), indicating Co oxidation. In contrast the *initial-BHAP shows little change in shape (edge energy 7119 eV and white line 7724 eV).

Co extended X-ray absorption fine structure (EXAFS) are shown in Figures S4 d-f. Fitting parameters (Table 2) for these reference samples (β-TCP and HAP-1) are slightly different. For Co adsorbed onto β-TCP, the Co–O distances of 2.02–2.05 Å are consistent with mainly 6-coordinate Co(II), but the distance of 1.94 Å for HAP-1 is more typical of a lower coordinated Co(II). The two reference samples (HAP-1 and β-TCP) show shells of phosphorus scatterers Co---P at 2.99–3.00 and 3.22–3.23 Å, respectively. The biogenic samples (initial-BHAP, 450-BHAP, 700-BHAP) all show a Co---P distance of 3.25–3.2; in addition, the spectrum of Co adsorbed onto 450-BHAP shows a significant contribution from P scatterers at 3.04 Å. For all three biogenic samples there is a peak in the Fourier transform at ca. 4.4 Å (Figure S3 h).

The EXAFS of the samples heated to 700 °C after Co sorption (denoted with *) show that the *initial-BHAP retained the Co–O shell at 2.01 Å. For the other heated sample (*HAP-1) the evidence of Co---P interaction is lost. For *HAP-1, in addition to Co–O at 1.92 Å, three shells of Co scatterers can be fitted at 2.86 Å, 3.37 Å, and 4.99 Å. This pattern of scatterers is typical of a spinel phase.[30] Temperature modification (700 °C) after metal sorption gave additional information on the site of incorporation. For *initial-BHAP and *HAP-1 there were changes in Co bonding when compared to the corresponding initial-BHAP and HAP-1, indicating that the bulk Co is incorporated into an inorganic amorphous phase that is changed during heat treatment (700 °C). For *HAP-1 it appears that Co is expelled during heat treatment and forms Co_xO_y clusters; such clusters were observed by El Kabouss[26] for HAP with adsorbed Co >1.7 g/100 g. For *initial-BHAP no Co scatterers appeared; however, the initial-BHAP sample contained 37% organic content with an estimated 20% of the adsorbed Co associated with this phase. It is therefore likely that a high proportion of this Co was lost during the sintering process.

Strontium XANES are shown in Figure S5 a-c; the spectra are comparable, with the same edge energy (16107) and white line (16113 eV), identical to the $Sr(CO_3)$ standard. However, the samples heated to 700 °C after Sr sorption (*HAP-1 and *initial-BHAP) and the 700-BHAP all show an increased intensity at ca. 16160 eV.

Strontium EXAFS (Figure S5 d-f) and associated Fourier transforms (Figure S5 g-i) show no similarities between the samples and strontium carbonate (Table 2). HAP-1 and β-TCP both have a single shell of oxygen scatterers at 2.58 and 2.57 Å. The initial-BHAP and 450-BHAP spectra also revealed similarities with a shell of oxygen scatterers at 2.58 Å and a shell of phosphorus scatterers at 3.26 Å. Characterization revealed that these materials have comparable properties (such as, smaller average crystallite size (<40 nm) and amorphous XRD patterns) so similar Sr bonding is expected. In contrast, the EXAFS results for 700-BHAP were very similar to the HAP data reported by Rokita et al.,[31] confirming Sr incorporation into the Ca(1)/Ca(2) position. Temperature modification (700 °C after metal sorption) gave additional information on Sr bonding. For the *initial-BHAP and *HAP-1 samples a shell of calcium scatterers appears (4.12–4.13 Å), indicating that Sr is incorporated within the bulk amorphous calcium phosphate phase and/or within the grain boundaries of HAP-1, an unstable phase which is modified by heat treatment.

Europium XANES showed that heating BHAP did not influence the site of europium incorporation. For all samples, the Eu L-edge XANES show similar spectra shapes (Figure S6 a-c).

Europium EXAFS (Figure S6 d-f) and Fourier transform (Figure S6 g-i) all show similar features and coordination information (a first shell of oxygens with a Eu–O bond length of 2.42–2.44 Å, a second shell of phosphorus scatterers at 3.18–3.20 Å, and a shell of europium scatterers at 4.10–4.21 Å) (Table 2). Previous research by Holliday et al.[11,32] showed similar EXAFS data (Eu–O 2.39 Å and Eu–P 3.21 Å), and additional analysis by TRLFS confirmed that *Cm* and Eu were not incorporated into the bulk crystalline HAP phase but associated with the amorphous grain boundaries. Herein, TCP or a similar mineral (a known mineral phase of the grain boundaries and it presence in BHAP has been confirmed by XRD analysis; Figure S2) is the likely site of incorporation with all spectra matching the β-TCP reference material. The Eu–O coordination number suggests Eu substitution at the Ca(2) and/or Ca(3) position of β-TCP. This is in agreement with Jay et al.,[13] who showed using atomic scale simulation that trivalent metals dopant with radii >0.9 Å show preference for the eight coordinated Ca(2) position of TCP. In this study, HAP-1 (with no detected TCP phase by XRD) showed poor sorption of Eu^{3+} (13 ± 3 mmol 100 g^{-1}) compared to 700-BHAP (151 ± 1 mmol 100 g^{-1}) which showed evidence of TCP content (Figure S2).

Remobilization of Incorporated Metals in Groundwater. Two amorphous (initial-BHAP and 450-BHAP) and a crystalline (700-BHAP) biogenic sample were tested to determine the stability of incorporated metals after 24 h contact time with groundwater (Table 3). For Co^{2+}, all BHAP samples (initial-BHAP, 450-BHAP, and 700-BHAP) remobilized similar amounts of sorbed Co^{2+} (<6.1%). Although there are differences in Co^{2+} loadings (initial-BHAP: 5.7 ± 0.1, 450-BHAP: 4.0 ± 0.1, and 700-BHAP: 1.0 ± 0.1 g/100 g Co^{2+}) for all samples, the amorphous calcium phosphate phase is the site of incorporation, thus, the percentage of remobilized Co^{2+} is also similar. For Sr^{2+}, the amorphous samples (initial-BHAP and 450-BHAP) showed the highest sorption (3.6 ± 0.1 and 2.9 ± 0.1 g/100 g, respectively). However, in these samples the site of incorporation was the less stable amorphous calcium phosphate phase, and up to 24% of the incorporated Sr^{2+} was remobilized in groundwater. The more crystalline (700-BHAP) sample absorbed up to 3 times less Sr^{2+} (1.3 ± 0.1 g/100 g), but this Sr was incorporated more stably (Ca(1) and/or Ca(2)

Table 3. Incorporated Metals (g/100g), % of Incorporated Metal Remobilized after 24 h in Groundwater and Proposed Site of Incorporation[a]

	initial-BHAP	450-BHAP	700-BHAP
Co^{2+} (g/100g)	5.7 ± 0.1	4.0 ± 0.1	1.0 ± 0.1
% remobilized	4.6	6.6	6.1
site of incorporation	amorphous calcium phosphate phase		
Sr^{2+} (g/100g)	3.6 ± 0.1	2.9 ± 0.1	1.3 ± 0.1
% remobilized	19.9	23.8	6.3
site of incorporation	amorphous calcium phosphate phase		Ca(1) and/or Ca(2) position of HAP
Eu^{3+} (g/100g)	23.4 ± 0.1	23.4 ± 0.1	23.0 ± 0.1
% remobilized	0	0	0
site of incorporation	Ca(2) and/or Ca(3) position of TCP		
U^{6+} (g/100g)	31.2 ± 0.1	31.3 ± 0. 1	27.6 ± 0.7
% remobilized	0.7	0.6	1.6
site of incorporation	surface complexed, no secondary precipitate		

[a]Error ± standard deviation and $N = 3$.

site of HAP) with only 6.3% remobilized in groundwater. Europium loadings were similar (23.3 ± 0.1 g/100 g) in all samples, and Eu^{3+} was stably incorporated into a β-TCP type mineral phase with no remobilization occurring within 24 h. Uranium loadings were also similar (31 ± 1.1 g/100 g) for all samples, and only a small portion of surface complexed UO_2^{2+} (<1.6%) remobilized in groundwater.

In summary, the higher sorption capacities for divalent radionuclides, multiple sites of radionuclide adsorption (surface complexation and incorporation into amorphous calcium phosphate, TCP, and crystalline HAP), and good stability against remobilization makes BHAP a promising material for radionuclide capture. The commercial HAP-1 material showed lower sorption of the divalent radionuclides and notable differences in the efficiency of (analogue Eu^{3+} and UO_2^{2+}) actinide sorption. The sorption of UO_2^{2+} onto HAP-1 was comparable to ≤600-BHAP due to similar surface area. However, HAP-1 had significantly lower (12 times) Eu^{3+} sorption, attributed to differences in TCP content. The 450-BHAP was established as the most suitable material for aqueous radionuclide remediation because any viable bacteria and the bulk organic content were removed while retaining the unique morphology and nanoscale properties that underlie increased radionuclide sorption capacity. The long-term stability of BHAP as a host for immobilized radionuclides is promising, especially for actinides (Eu^{3+} analogue for trivalent actinides and UO_2^{2+}) with up to 31 g/100 g incorporated and less than 2% remobilized in groundwater.

ASSOCIATED CONTENT

Supporting Information

XRD patterns, SEM and TEM images, XANES and EXAFS spectra, and XRD patterns. This material is available free of charge via the Internet at http://pubs.acs.org.

AUTHOR INFORMATION

Corresponding Author

*E-mail: s.handley-sidhu@bham.ac.uk.

Notes

The authors declare no competing financial interest.

ACKNOWLEDGMENTS

This work was jointly funded by the Engineering and Physical Sciences Research Council (EPSRC) and Natural Environment Research Council (NERC) grant (EP/G063699/1) with the support of the Diamond Light Source and the NERC Facility for Environmental Nanoscience Analysis and Characterisation. We would also like to thank Louise Male, Jackie Deans, and Fred Mosselmans for their technical support and input into this project.

REFERENCES

(1) Oelkers, E. H.; Montel, J. M. Phosphates and nuclear waste storage. *Elements* **2008**, *4*, 113−116.

(2) Handley-Sidhu, S.; Renshaw, J. C.; Yong, P.; Kerley, R.; Macaskie, L. E. Nano-crystalline hydroxyapatite bio-mineral for the treatment of strontium from aqueous solutions. *Biotechnol. Lett.* **2011**, *33*, 79−87.

(3) Simon, F. G.; Biermann, V.; Segebade, C.; Hedrich, M. Behaviour of uranium in hydroxyapatite-bearing permeable reactive barriers: investigation using ^{237}U as a radioindicator Sci. *Total Environ.* **2004**, *326*, 249−256.

(4) Macaskie, L. E.; Dean, A. C. R. Cadmium accumulation by a *Citrobacter* sp. *J. Gen. Microbiol.* **1984**, *130*, 1855−1867.

(5) Thackray, A. C.; Sammons, R. L.; Macaskie, L. E.; Yong, P.; Marquis, P. M. Bacterial biosynthesis of calcium bone-substitute material. *J. Mater. Sci. Mater. Med.* **2004**, *15*, 403−406.

(6) Handley-Sidhu, S.; et al. Uptake of Sr^{2+} and Co^{2+} into Biogenic Hydroxyapatite: Implications for biomineral ion exchange synthesis. *Environ. Sci. Technol.* **2011**, *45*, 6985−6990.

(7) Xie, B.; Nancollas, G. H. How to control the size and morphology of apatite nanocrystals in bone. *Proc. Natl. Acad. Sci. U. S. A.* **2010**, *107*, 22369−22370.

(8) Gorden, L. M.; Lawrence, T.; Joester, D. Atom probe tomography of apatites and bone-type mineralized tissues. *ACS Nano* **2012**, *6*, 10667−10675.

(9) Nakano, T.; et al. Change in microstructure and solubility improvement of HAp ceramics by heat-treatment in a vacuum. *Mater. Trans.* **2002**, *43*, 3105−3111.

(10) Terra, J.; et al. The structure of strontium-doped hydroxyapatite: an experimental and theoretical study. *Phys. Chem. Chem. Phys.* **2009**, *11*, 568−577.

(11) Holliday, K.; et al. A new incorporation mechanism for trivalent actinides into bioapatite: A TRLFS and EXAFS study. *Langmuir* **2012**, *28*, 3845−3851.

(12) Gregori, G.; Kleebe, H. J.; Mayr, H.; Ziegler, G. EELS characterisation of B-tricalcium phosphate and hydroxyapatite. *J. Eur. Ceram. Soc.* **2006**, *26*, 1473−1479.

(13) Jay, E. E.; Mallinson, P. M.; Fong, S. K.; Metacalfe, B. L.; Grimes, R. W. Partitioning of dopant cations between β-tricalcium phosphate and fluorapatite. *J. Nucl. Mater.* **2011**, *414*, 367−373.

(14) Brookshaw, D. R.; Pattrick, R. A. D.; Lloyd, J. R.; Vaughan, D. J. Microbial effects on mineral-radionuclide interactions and radionuclide solid-phase capture processes. *Mineral. Mag.* **2012**, *73*, 777−806.

(15) Ledo, H. M.; et al. Microstructure and composition of biologically synthesized hydroxyapatite. *J. Mater. Sci. Mater. Med.* **2008**, *19*, 3419−3427.

(16) Patterson, A. L. The Scherrer formula for X-ray particle size determination. *Phys. Rev.* **1939**, *56*, 978−982.

(17) Gustafsson, J. P. USEPA's Visual MINTEQ ver. 3.0/3.1 [software], 2000. Available from http://vminteq.lwr.kth.se/ (accessed May 19, 2014).

(18) Gurman, S. J.; Binsted, N.; Ross, I. A rapid, exact, curved-wave theory for EXAFS calculations. *J. Phys. C* **1984**, *17*, 143−151.

(19) Tomic, S. et al. New Tools for the Analysis of EXAFS: The DL EXCURV Package, CCLRC Technical Report DL-TR-2005-001, ISSN 1362-0207 (2005).

(20) Hedin, L.; Lundqvist, S. Effects of electron-electron and electron-phonon interactions on the one-electron states of solids. *Solid State Phys.* **1969**, *23*, 1−181.
(21) Binsted, N.; Strange, R. W.; Hasnain, S. S. Constrained and restrained refinement in EXAFS data analysis with curved wave theory. *Biochemistry* **1992**, *31*, 12117−12125.
(22) Fuller, C. C.; Bargar, J. R.; Davis, J. A.; Piana, M. J. Mechanism of uranium interactions with hydroxyapatite: implications for groundwater remediation. *Environ. Sci. Technol.* **2002**, *36*, 158−165.
(23) Cuthbert, M. O.; et al. Controls on the rate of ureolysis and the morphology of carbonate precipitated by S. *Pasteurii* biofilms and limits due to bacterial encapsulation. *Ecol. Eng.* **2012**, *41*, 32−40.
(24) Kajander, O. E.; Ciftcioglu, N. Nanobacteria: An alternative mechanism for pathogenic intra- and extracellular calcification and stone formation. *Proc. Natl. Acad. Sci. U. S. A.* **1998**, *95*, 8274−8279.
(25) Sasaki, K.; et al. Ion exchange capacity of Sr^{2+} onto calcined biological hydroxyapatite and implications for use in permeable reactive barriers. *Mater. Trans., JIM* **2012**, *53*, 1267−1272.
(26) El Kabouss, K.; et al. Cobalt speciation in cobalt oxide-apatite materials: structure-properties relationship in catalytic oxidative dehydrogenation of ethane and butan-2-ol conversion. *J. Mater. Chem.* **2006**, *16*, 2453−2463.
(27) Shannon, R. D. Revised effective ionic radii and systematic studies of interatomic distances in halides and chalcogenides. *Acta Crystallogr., Sect. A* **1976**, *32*, 751−761.
(28) Luo, Y.; Hughes, J. M.; Rakovan, J.; Pan, Y. M. Site preference of U and Th in Cl, F, and Sr apatites. *Am. Mineral.* **2009**, *94*, 345−351.
(29) Fuller, C. C.; Bargar, J. R.; Davis, J. A. Molecular-scale characterization of uranium sorption by bone apatite materials for a permeable reactive barrier demonstration. *Environ. Sci. Technol.* **2003**, *37*, 4642−4649.
(30) Henderson, C. M. B.; Charnock, J. M.; Plant, D. A. Cation occupancies in Mg, Co, Ni, Zn-ferrite spinels: a multi-element EXAFS study. *J. Phys.: Condens. Mater.* **2007**, *19*, 076214.
(31) Rokita, E.; Hermes, C.; Nolting, H. F.; Ryczek, J. Substitution of calcium by strontium within selected calcium phosphates. *J. Cryst. Growth* **1993**, *130*, 543−552.
(32) Holliday, K.; Dardenne, K.; Walther, C.; Stumpf, T. The Incorporation of Europium into Apatite: A new explanation. *Radiochim. Acta* **2013**, *101*, 267−272.